RSC Applied Interfaces

Accepted Manuscript

This article can be cited before page numbers have been issued, to do this please use: A. Darda, N. N. Gosvami and W. A. Siddiqi, *RSC Appl. Interfaces*, 2026, DOI: 10.1039/D6LF00075D.

ROYAL SOCIETY OF CHEMISTRY

rsc.li/RSCApplInter

View Article Online
DOI: 10.1039/D6LF00075D

Synergistic Effect of WO_3 on Physico-chemical, Physico-mechanical, Hydrophobic, and Anticorrosive Performance of Poly-(*melamine-co-formaldehyde)*-Cured *Pithecellobium dulce*-Alkyd Nanocomposite Coatings

Abu Darda[1*], Nitya Nand Gosvami[1], Weqar Ahmad Siddiqi[2]

[1]*Department of Materials Science and Engineering, Indian Institute of Technology, Delhi*

[2]*Department of Applied Sciences and Humanities, Jamia Millia Islamia, New Delhi*

Abstract

The development of sustainable and environmentally friendly nanocomposite coatings for advanced corrosion protection has gained significant attention in modern coating technology. In this study, a bio-based alkyd nanocomposite coating was developed from *Pithecellobium dulce* seed oil-derived alkyd (PDA), cured with poly-(melamine-co-formaldehyde)-isobutylated resin (PMF_{80}), and reinforced with tungsten trioxide (WO_3) nanofillers. Different WO_3 loadings (0.25–1.25 wt.%) were investigated, and 1.0 wt.% WO_3 exhibited the best overall performance. The nanocomposites were synthesized through an in-situ polymerization approach and applied onto carbon steel (CS) substrates by brush coating. Structural, thermal, morphological, and surface properties were analyzed using FTIR, NMR, TGA, TEM, AFM, and contact angle measurements. Electrochemical anticorrosive performance was evaluated in 5 wt.% NaCl solution using Potentiodynamic Polarization (PDP) and Electrochemical Impedance Spectroscopy (EIS) techniques. The WO_3@PDA-PMF_{80} coating demonstrated enhanced hydrophobicity, thermal stability, adhesion strength, and surface compactness compared with PDA and PDA-PMF_{80} coatings. AFM studies confirmed lower surface roughness variation after corrosion exposure, indicating improved barrier characteristics. The optimized coating exhibited excellent corrosion protection efficiency (η_i) of 99.99% and a very low corrosion rate of 4.81×10^{-4} mpy. The enhanced performance was attributed to improved crosslink density,

View Article Online
DOI: 10.1039/D6LF00075D

homogeneous WO_3 dispersion, and tortuous diffusion pathways that restricted electrolyte penetration.

Keywords: *Pithecellobium dulce* Seed Oil, oil-derived alkyd, WO_3 Nanofillers, Potentiodynamic Polarization (PDP), Electrochemical Impedance Spectroscopy (EIS), Anticorrosive, Sustainable, Nanocomposite Coatings

1 Introduction

Corrosion is a thermodynamically driven phenomenon that occurs through chemical or electrochemical reactions, resulting in significant degradation of materials. This process results in substantial economic losses at both national and international levels [1,2], affecting various industries that rely on metal-based infrastructure, including the transportation, energy, and construction sectors. As a natural process, corrosion cannot be entirely eradicated; however, it can be significantly mitigated through various strategies, including alloying, periodic cleaning, optimized design, inhibitors, and coatings [3–6]. Among these methods, the application of coatings has attracted widespread attention due to their accessibility, reasonable cost, and better protection ability to industrial assets. Despite the advantages of coatings, conventional approaches often involve excessive organic solvents that emit volatile organic compounds (VOCs) [7,8]. VOCs are hazardous to human health, contribute to environmental pollution, and are subject to stringent regulations. The coatings industry is thus under pressure to develop sustainable alternatives that reduce VOC emissions while maintaining the functional properties required for protection in corrosive environments. Additionally, traditional monomeric materials used in the production of coatings often rely on fossil fuels, a non-renewable resource expected to be depleted shortly.

View Article Online
DOI: 10.1039/D6LF00075D

These concerns have spurred research into renewable, eco-friendly monomeric materials, such as lignin, chitin, cashew nut shell oil, and various vegetable seed oils [9–11]. Vegetable oils (VOs), in particular, have emerged as promising candidates for the synthesis of sustainable polymers. VOs such as castor, linseed, soy, palm, tung, pongamia, sunflower, safflower, and *Pithecellobium dulce* oil (PDO) have been successfully used to produce a variety of bio-based polymers, including oleo-polyurethanes, oleo-polyesteramides, oleo-polyetheramides, oleo-epoxies, oleo-polyacrylates, and oleo-alkyds [11–15]. Among these, oleo-alkyds are of particular interest due to their low molecular weight, excellent fluidity, and ability to form sphere-shaped macromolecules that spread easily on substrates without the need for VOCs. These properties have led to the development of oleo-alkyd coatings that are not only low-VOC but also demonstrate excellent adhesion and protection [16]. Since the early 1940s, oleo-alkyds have been used to produce coatings and currently account for more than 50% of all oleo-polymers employed in these applications. Their versatility and environmental benefits have made them a popular choice for various surface coating technologies. Recent studies have explored the potential of hybrid nanocomposites to enhance the performance of oleo-alkyd coatings. For instance, J. R. Xavier et al. discussed the anticorrosive properties of WO_3 modified epoxy coatings[17], A. Darda et al. PDO-based polyesteramide nanocomposite coatings and discussed their anticorrosive properties [16], while Selim et al. [18] reported the development of linseed oil-based alkyd/Cu_2O nanocomposite coatings for surface protection applications. Despite these advances, there has been limited research on the anticorrosive properties of polymer coatings derived from PDO. This gap in the literature presents an opportunity to explore the use of PDO-based alkyd coatings, particularly in the development of nanocomposites reinforced with metal oxide nanofillers. Among the various nanofillers explored in oleo-alkyd systems, metal oxides such as Fe_3O_4, V_2O_5, CeO_2, SiO_2, and

View Article Online
DOI: 10.1039/D6LF00075D

WO_3 have shown considerable promise [12,14,17,19–22]. WO_3, in particular, exhibits good compatibility and can be uniformly dispersed within polymer matrices, contributing to improved mechanical robustness and enhanced barrier properties. The electrostatic interactions between the WO_3 nanofillers and the polymer matrix, resulting in a dense network and surface roughness, further support the hydrophobic behavior and EC resistance abilities of the coating. Oleo-alkyds having functional groups such as carboxyl and hydroxyl are particularly well-suited to interact with WO_3 metal oxides [17]. This interaction results in the formulation of a well-adhered, high cross-linked, and non-poisonous material that exhibits higher wettability, excellent physicochemical, physico-mechanical properties, and promising electrochemical stability compared to traditional coatings [22,23].

Recognizing this potential, the present work reports the development of a novel PDO-based alkyd (PDA), along with a poly-(melamine-co-formaldehyde)-isobutylated solution (PMF)-cured PDA (PDA-PMF_{80}), and a WO_3 nanofiller-dispersed PDA-PMF_{80} (WO_3@PDA-PMF_{80}) nanocomposite. The synthesis of these nanocomposite coatings was achieved via an in-situ polymerization process. Their structural, morphological, and thermal characterizations were performed using a variety of techniques, including Fourier-transform infrared (FTIR) spectroscopy, Nuclear Magnetic Resonance (NMR) spectroscopy, Scanning Electron Microscopy (SEM), Transmission Electron Microscopy (TEM), Thermo-gravimetric Analysis (TGA), and contact angle (CA) analysis. The PDA and its nanocomposite coatings were then applied to carbon steel (CS) specimens to evaluate their physicochemical and anti-corrosive performance. Their EC protection performances were explored with the help of potentiodynamic polarization (PDP) and electrochemical impedance spectroscopy (EIS). Specifically, the WO_3@PDA-PMF_{80} coatings demonstrated a corrosion potential (E_{corr}) of -0.52804 V, a

View Article Online
DOI: 10.1039/D6LF00075D

corrosion current density (I_{corr}) of 1.56×10^{-7} A/cm^2, corrosion protection efficiency (η_i) of 99.99%, and a corrosion rate of 4.81×10^{-4} mpy, indicating an excellent resistance to corrosion under 5 weight % aqueous NaCl solution. The incorporation of WO_3 nanofillers within the PDA matrix enhanced the hydrophobicity and adhesion of the WO_3@PDA-PMF_{80} nanocomposite coatings. The studies demonstrate that WO_3@PDA-PMF_{80} nanocomposite coatings provide significantly better electrochemical corrosion (EC) protection than bare PDA coatings and other similar coating systems documented in the literature.

2 Experimental Sections

2.1 Materials

PMF: [refractive index:1.468, boiling point: 108 °C, molecular weight: ~ 1620, density: 1g/ml] and Tetrachlorophthalic anhydride (TCPA) [molecular weight: 148.1 g mol-1, Purity: 98%] were obtained from Sigma Aldrich. P-Toluene sulfonic acid (p-TSA) was procured from Loba Chemical, Mumbai, India, while Sodium tungstate ($Na_2WO_4.2H_2O$), Hydrogen peroxide (H_2O_2, 30 wt. %), Ethanol (C_2H_5OH), Glycerol ($C_3H_8O_3$ 98%), Diethyl ether $(C_2H_5)_2O$, and Acetone (CH_3COCH_3) were procured from Merck India. PDO and different grades of silicon carbide (SiC) papers (120, 180, 320, and 480) were obtained from the local market. Sodium hydroxide (NaOH 97%), Sodium chloride (NaCl 99%), Sodium sulfate (Na_2SO_4), and Sodium bicarbonate ($NaHCO_3$) were purchased from Fisher Scientific (Mumbai, India). CS specimens (0.87% C, 97.13% Fe in wt. %) were supplied by Reliable Metal Works, Mumbai, India. These materials were used as received.

View Article Online
DOI: 10.1039/D6LF00075D

2.2 Synthesis of WO_3 nanoparticles

In accordance with a previously documented protocol, the WO_3 nanoparticles were created via in-situ method [24]. To create a clear and transparent solution mixture, 10 ml of 6.8% H_2O_2 solution was mixed with 3.3 g of $Na_2WO_4.2H_2O$ and agitated for 2.5 hours. A dark yellow solution developed as a result of heating the solution mixture for two hours at 61-63°C. A light green precipitate of WO_3 nanoparticles formed as a result of the dark yellow solution being left to react overnight at room temperature while being constantly stirred. Centrifugation was then used to separate the precipitate, which was subsequently cleaned with ethanol and deionized (DD) water. The resulting WO_3 powder was further dried at 60°C overnight. FTIR and TEM analyses of the dried powder verified that WO_3 nanoparticles were successfully formed [25].

2.3 Synthesis of monoglyceride derived from *Pithecellobium dulce* oil (PDMG)

PDMG was synthesized using the previously described procedure [26]. In summary, a four-neck flat-bottomed flask was filled with PDO (5 mol), $C_3H_8O_3$ (0.05 mol), and NaOH (0.01 mol) at a molar ratio of 1:2:0.01. To keep the reaction environment under control, the system included a thermometer, a nitrogen intake, and a magnetic stirrer. For 1.5 hours, the reaction mixture was constantly stirred at 160-180°C. The reaction's progress was monitored using the acid test, and FT-IR spectra were recorded at regular intervals. When the reaction product (PDMG) reached the required acid value, the reaction was stopped. The successful synthesis of PDMG was validated by the FTIR measurement and the desired acid value. PDMG was then dissolved in $(C_2H_5)_2O$ solution for its purification. The solution was then washed with Na_2SO_4 (anhydrous solution), followed by passing with $NaHCO_3$ to remove the unreacted moieties of fatty acids and

View Article Online
DOI: 10.1039/D6LF00075D

moisture. Finally, the trapped ether was evaporated under vacuum, resulting in the purified PDMG for further use.

2.4 Synthesis of PDO-based alkyd (PDA) and PMF-cured PDA nanocomposite (PDA-PMF_{80})

According to the previous procedure, PDA was developed by reacting PDMG with TCPA [26]. To put it briefly, a magnetic stirrer was used to maintain the solution mixture of PDMG (1 mole) and TCPA (0.5 moles) in a round-bottomed flask. For one and a half hours, the reaction mixture was constantly stirred up to 180°C. The FT-IR spectroscopic method was used to periodically check on the reaction's progress. To obtain the final product (PDA), the reaction was halted when the required acid value (0.025 mg KOH/g) was reached. PDA was successfully synthesized when the reaction product was cooled to 55°C and triethylamine was added to the reaction solution to neutralize the free terminal carboxylic groups. To get rid of any remaining moisture, the manufactured PDA was first cleaned with a 15% aqueous solution of NaCl, then twice or three times with distilled water, and then dried with anhydrous Na_2SO_4.

PMF was added to ethanol (a green solvent) in different weight percentages (60%, 70%, 80%, and 100%) to cure the PDA matrix. The curing reaction was aided by the employment of the p-TSA as a catalyst. The reaction solution was conducted at 110°C for 2.5 hours while being continuously stirred in the pH range of 5-6. The FTIR spectroscopic approach was used to continuously monitor the curing reaction's progress until the characteristic FTIR peak (-OH and C=O) reached a constant strength (Figure 1). PMF weight ratios of 100:30, 100:50, 100:70, and 100:80 was investigated for PDA resin curing. The PDA-PMF_{80} with 100:80 ratios showed the finest physico-mechanical characteristics among them. WO_3 nanofiller-dispersed PDA-PMF_{80}

View Article Online
DOI: 10.1039/D6LF00075D

nanocomposites were formulated by further processing this PDA-PMF_{80} (Table S-2 and Figure 5).

2.5 Formulation of WO_3-dispersed PDA-PMF_{80} nanocomposite (WO_3@PDA-PMF_{80})

In-situ polymerization methods were used to formulate WO_3@PDA-PMF_{80} nanocomposites. Using the same procedure described in the previously mentioned section (Section 2.4), the ethanol solution of PDA and PMF was made in a 100:80 w/w ratio. Next, two to three drops of p-TSA cross-linker (as a catalyst) were added to the reaction mixture (PDA-PMF_{80}). The second stage involved dispersing different weight percentages of WO_3 nanoparticles (0.25, 0.50, 0.75, 1.00, and 1.25 weight percent) in the PDA-PMF_{80} ethanolic solution for 2.5 hours at 120°C while stirring continuously. The full curing of nanocomposite coatings was not possible, however, up to 0.75% dispersion; coatings dried in 25-35 minutes above this rate. The best physico-mechanical properties have been demonstrated by coatings with a 1.0% dispersion of nanofillers, whereas coatings with a 1.25% dispersion cure quickly but are unstable. Therefore, 1.0 wt.% of WO_3 nanoparticles were dispersed in ethanol for 2.5 h. This dispersion was then added to the PDA-PMF_{80} matrix and further stirred for 1.5 h at 120°C to ensure the uniform incorporation of WO_3 nanofillers within the PDPA-PMF_{80} matrix, resulting in the formulation of WO_3@PDA-PMF_{80} nanocomposites (Figure-1d, Figure 4b, and Scheme-1).

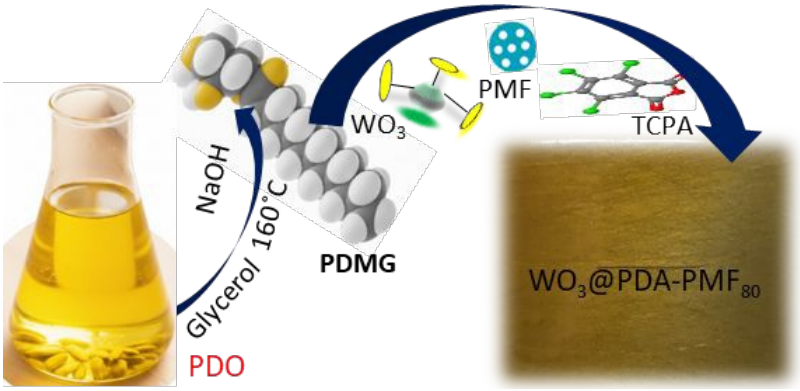

View Article Online
DOI: 10.1039/D6LF00075D

Scheme 1: Diagrammatic illustration of the monoglyceride-based production of PDO-derived PMF-cured alkyd nanocomposites supplemented with WO_3 nanofillers (WO_3@PDA-PMF_{80}).

2.6 Fabrication of coatings on CS substrates

The surface of finely polished CS (0.87 weight percent C and 97.13 weight percent Fe) specimens was coated with a homogeneous solution of the PDA, PDA-PMF_{80}, and WO_3@PDA-PMF_{80} nanocomposite coatings. Different grades of SiC sheets (120, 180, 320, and 480 mesh sizes)[27] were used to polish the commercially available CS strips of different standard sizes. They were then thoroughly cleaned and rinsed with water, C_2H_5OH, and $(CH_3)_2C{=}O$ before being allowed to air dry. After being ultrasonically cleaned with deionized water and an ethanol-acetone blend solution, the CS specimens were rinsed with CCl_4 and allowed to dry for two and a half hours at room temperature. Then, using the brush approach, the homogeneous solution of PDA, PDA-PMF_{80}, and WO_3@PDA-PMF_{80} nanocomposites was applied to the surface of CS strips that had been finely polished. These materials were coated on CS strips measuring 70 mm by 25 mm by 1 mm for physico-mechanical testing and 25 mm by 25 mm by 1 mm for EC resistance testing and morphological investigations.

2.7 Characterization

The physicochemical analyses [specific gravity (g/ml at 25˚C), acid value (mg KOH/g), refractive index (25˚C), spectroscopic (FT-IR and NMR), morphological (SEM and TEM), thermal (TGA) characterization, anticorrosive (PDP and EIS) performances, and physicomechanical tests [impact (250, lb.inch-1), scratch hardness (Kg), bend (1/8"inch), cross-

View Article Online
DOI: 10.1039/D6LF00075D

hatch, DTT (min), DTH (h), gloss (45^{o}), and coating thickness (μm)] were carried out in accordance with their ASTM standards.

Using the Shimadzu FTIR Affinity-I model, FT-IR spectroscopic techniques were used to examine the molecular structures of the WO_3 nanoparticles, bare PDA, PDA-PMF_{80}, and WO_3@PDA-PMF_{80} nanocomposites over a 400-4000 cm^{-1} range. Additionally, solid-state ^{1}H NMR spectroscopy employing a Bruker Advance III 500 MHz NMR was used to elucidate the structure of PDA-PMF_{80}. The impact resistance [ASTM-D2794], scratch hardness [ASTM-D3363], bend test [ASTM-D522], cross-hatch test [ASTM-D3359], gloss [ASTM C346], and DTT/DTH [ASTM D1640] of bare PDA, PDA-PMF_{80}, and WO_3@PDA-PMF_{80} coatings were all tested [12,14,26,28]. An Elcometer was used to measure the coating thickness (ASTM-B499). Transmission electron microscopy (TEM FEI Technai F-30, Holland) was used to examine the dispersion pattern of nanofillers inside the PDA matrix, while FE-SEM (ZEISS Ultra 55, Germany) was used to examine the morphology of uncoated and coated CS specimens. Following the cross-hatch test, the optical micrographs of these nanocomposite coatings were also captured using a Lietz optical microscope (Model Metallux-3). However, a thermogravimetric analyzer (NETZSCH; STA 449 F-1 Jupiter) was used to examine their thermal stabilities. 4-6 mg of the final powdered sample was prepared and deposited onto the sample holder (a platinum pan) for TGA analysis. The experiments were carried out with a purging rate of 40 mL/min and a scan rate of 10˚C min^{-1} in the 30-800˚C range under N_2 flow.

The EC resistance performance of uncoated CS, PDA, and its corresponding nanocomposite coatings was evaluated using a Potentiostat/Galvanostat (Micro-Autolab Type III, 3-A-VT-70762, Netherlands). The measurements were carried out in a conventional three-electrode electrochemical cell configuration consisting of Ag/AgCl as the reference electrode, platinum

View Article Online
DOI: 10.1039/D6LF00075D

gauze as the auxiliary (counter) electrode, and the coated/uncoated specimen as the working electrode. The electrodes were assembled in an EG&G glass cell with a capacity of 400 mL, containing 5 wt.% NaCl solution as the corrosive electrolyte. A fixed exposure area of 1 × 1 cm² of the working electrode was immersed in the electrolyte at room temperature and allowed to stabilize for 15 min before measurements. The open circuit potential (OCP) was recorded for 600 s to ensure system stabilization. EIS measurements were conducted in the frequency range of 100 kHz to 0.1 Hz with a sinusoidal perturbation amplitude of 10 mV under the saline environment (5 wt.% NaCl). The corrosion parameters, including I_{corr} and E_{corr}, were further determined using potentiodynamic polarization (PDP) tests performed within a potential range of ±100 mV relative to OCP at a scan rate of 0.01 mV s^{-1}. The impedance data were analyzed and fitted using NOVA software (version 1.10) to obtain the equivalent circuit parameters.

3 Results and Discussion

3.1 FTIR analysis

FT-IR spectroscopy was employed to confirm the formation of WO_3 nanoparticles (Figure S-1), PDMG, bare PDA, PDA-PMF_{80}, and WO_3@PDA-PMF_{80} nanocomposites (Figure-1. a-d). The FTIR spectrum of WO_3 nanoparticles is discussed in detail in the supporting information (Section S-1 and Figure S-1). However, the FT-IR spectrum of PDMG is depicted in Figure-1a, which describes the peak at 3433.26 cm^{-1} attributed to the $^{-}$OH (stretching) of monoglyceride and the similar bands with their lower intensities indicate the successful formation of PDA, PDA-PMF_{80}, and WO_3@PDA-PMF_{80} respectively[7,29]. In the FT-IR spectrum of PDA (Figure-1b), a band appears at 1740.20 cm^{-1}, corresponding to the ester linkage. Peaks at 2922.87 cm^{-1} and 2851.71 cm^{-1} are attributed to the symmetric/asymmetric stretching of $-CH_3$ and $-CH_2$ groups within the fatty acid chain of PDA [29]. In the FT-IR spectrum of the PDA$-PMF_{80}$ (Figure-

View Article Online
DOI: 10.1039/D6LF00075D

1c), the characteristic peaks at 1553.08 cm^{-1}, 1087.69 cm^{-1}, and 1481.86 cm^{-1} corresponded to the s-triazine ring of PMF (stretching), −C−O−C− (stretching and bending), and −C−H (deformations), respectively, confirming the successful incorporation of PMF into the PDA matrix[30]. These peaks imply that the -OH group of PDMG reacts with an acid group of TCPA to develop PDA.

However, the FT-IR spectrum of WO_3@PDA-PMF_{80} (Figure-1d) exhibits similar characteristic peaks with comparatively lower intensity than PDA-PMF_{80}. Such reduction in intensity at 656.68 cm^{-1} and 807.81 cm^{-1} may be attributed to the incorporation of WO_3 nanofillers within the PDA-PMF_{80} matrix, resulting in partial dilution of the organic phase along with possible interfacial interactions between the WO_3 nanoparticles and the polymeric backbone/interstitial regions of the matrix, without significantly altering the basic chemical structure of the polymer network.[22,31,32]

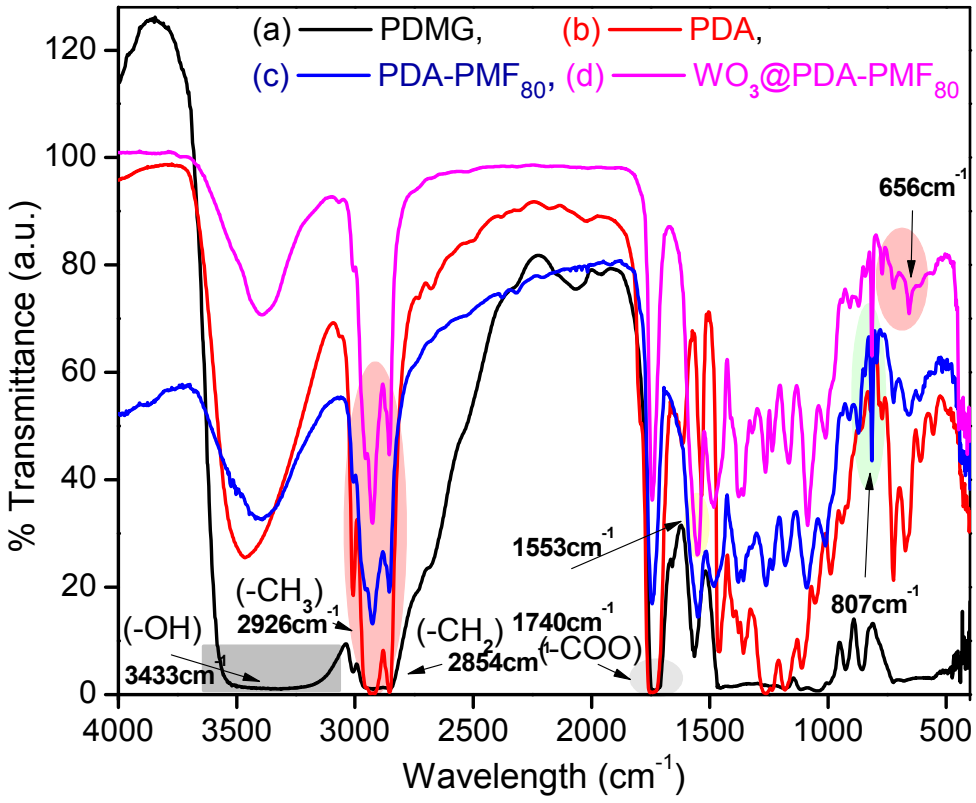

View Article Online
DOI: 10.1039/D6LF00075D

Figure-1 FTIR spectra of (a) PDO-derived monoglyceride (PDMG), (b) PDMG-based alkyd (PDA), (c) PMF_{80}-cured alkyd (PDA-PMF_{80}), and (d) WO_3-dispersed PDA-PMF_{80} nanocomposites (WO_3@PDA-PMF_{80}).

3.2 NMR analysis

The structural details of PDA-PMF_{80} were extensively characterized through ^{1}H NMR and ^{13}C solid-state NMR spectroscopy, as illustrated in Figure-2. In the ^{1}H NMR spectrum of PDA-PMF_{80} (Figure-2a), the signals at δ = 0.84–0.88 ppm and δ = 1.23–1.28 ppm are attributed to the terminal $–CH_3$ and methylene ($–CH_2–$) protons of the long fatty acid chains, confirming the aliphatic backbone of the resin. The resonance at δ = 1.58–1.59 ppm corresponds to protons adjacent to olefinic groups (–CH=CH–). The peak observed at δ = 1.98–2.04 ppm is assigned to aromatic protons associated with the benzene ring. The signal at δ = 2.28–2.31 ppm is attributed to methylene protons adjacent to ester linkages ($–CH_2–O–C=O$). The resonance at δ = 2.73–2.76 ppm indicates the presence of residual hydroxyl (–OH) protons. The signal at δ = 3.64–3.71 ppm corresponds to methylene groups positioned between two olefinic carbon atoms within the fatty acid chain. The peaks in the range δ = 4.09–4.46 ppm are assigned to methylene protons adjacent to ester functionalities, while the signal at δ = 5.06 ppm represents protons of fatty acid chains neighboring ester-linked $–CH_2$ groups. The resonance at δ = 5.30–5.36 ppm confirms the presence of unsaturated (C=C) protons in the fatty acid chains. Furthermore, the signal at δ = 7.26 ppm verifies the aromatic protons derived from TCPA incorporated within the PDA matrix. These characteristic signals collectively confirm the successful synthesis of PDA-PMF_{80}.

The ^{13}C solid-state NMR spectrum of PDA-PMF_{80} (Figure-2b) further supports the proposed structure. The signals in the range δ = 14.71–30.05 ppm correspond to methyl ($–CH_3$) and

View Article Online
DOI: 10.1039/D6LF00075D

methylene (–CH_2–) carbons of the aliphatic glyceride chain, confirming the fatty acid backbone. The peak at δ = 67.07 ppm is attributed to carbon atoms associated with olefinic (CH=CH) groups, indicating the presence of unsaturation within the resin structure. The resonance at δ = 132.53 ppm corresponds to aromatic carbons originating from tetrachlorophthalic anhydride. The peak at δ = 166.72 ppm is assigned to the carbon atoms of the s-triazine ring, confirming the incorporation of the melamine-derived aromatic structure into the PDA network. Finally, the signal at δ = 173.17 ppm corresponds to the ester carbonyl (C=O) carbons, confirming the formation of ester linkages in the PDA-PMF_{80} system. [7,30]

View Article Online
DOI: 10.1039/D6LF00075D

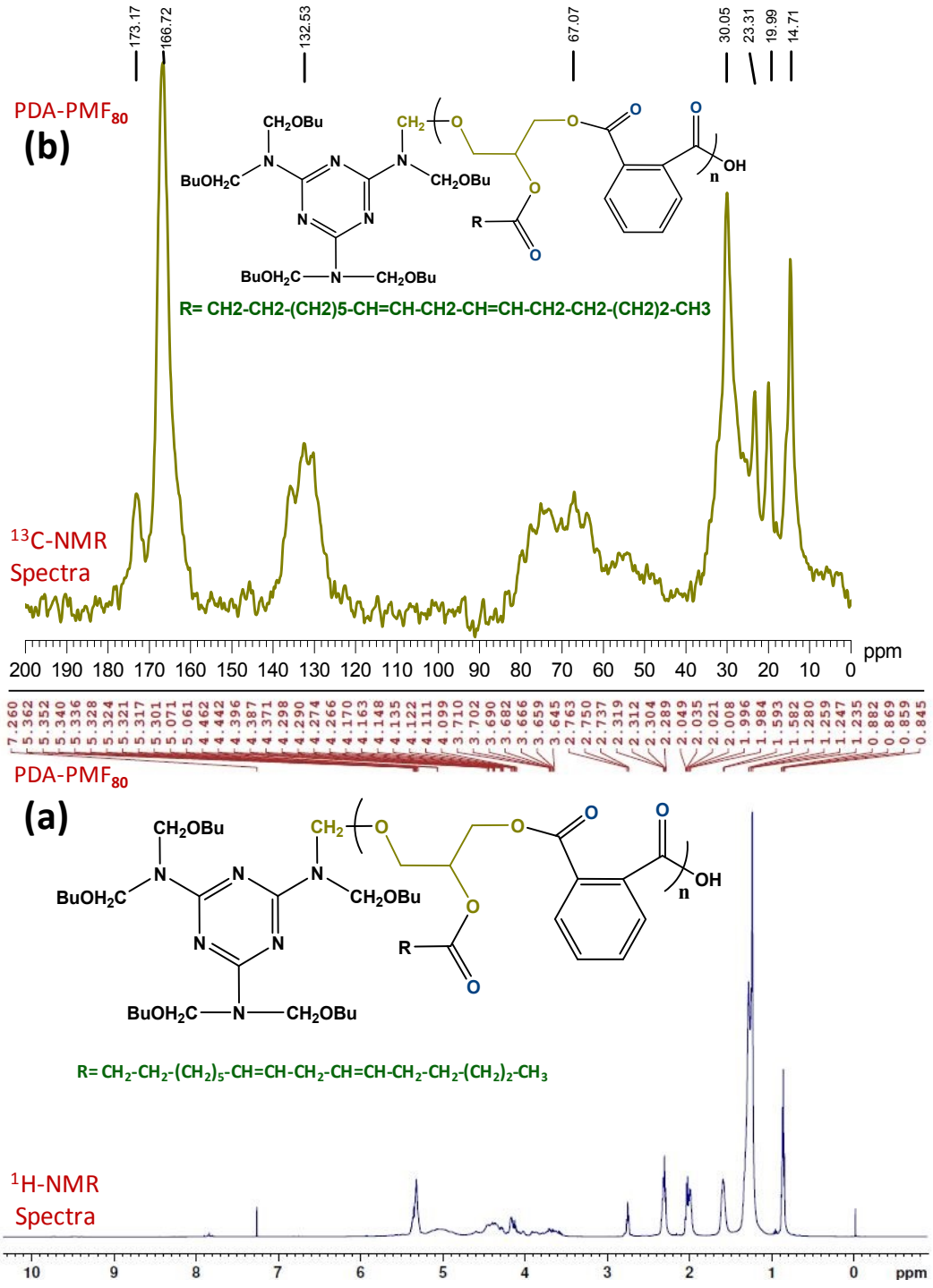

Figure-2 (a) Proton (^{1}H) NMR and (b) Carbon (^{13}C) solid-state NMR spectra confirming the structural characteristics of PMF-cured PDA (PDA-PMF$_{80}$).

View Article Online
DOI: 10.1039/D6LF00075D

3.3 TGA analysis

Thermogravimetric analysis (TGA) was carried out to evaluate the thermal degradation behavior and thermal stability of PDA-PMF_{80} and WO_3@PDA-PMF_{80} nanocomposite coatings under a nitrogen atmosphere (Figure-3, and Table S-3). The comparative thermograms and the derived thermal parameters clearly demonstrate the positive influence of WO_3 nanofiller incorporation on the thermal resistance of the polymer matrix.

An initial minor weight loss was observed below ~150 °C for both coatings, corresponding to the removal of physically adsorbed moisture and residual volatile/solvent molecules entrapped within the polymeric network. The PDA-PMF_{80} coating exhibited an initial decomposition temperature (IDT) around 136 °C, while WO_3@PDA-PMF_{80} showed a slightly delayed decomposition onset near 138 °C, indicating marginal improvement in the initial thermal resistance after WO_3 incorporation[7].

The major thermal degradation of PDA-PMF_{80} started around 304 °C, corresponding to approximately 5 wt.% weight loss (T_d5/T_5), which is associated with the cleavage and decrosslinking of the cross-linked polymeric framework[29]. In contrast, the WO_3@PDA-PMF_{80} nanocomposite exhibited a noticeable shift of the degradation region toward higher temperatures (~336 °C), confirming improved thermal stability due to the incorporation of WO_3 nanofillers. Similar enhancement in degradation temperature has been previously reported for Fe_3O_4- and RGO-reinforced alkyd nanocomposite systems, where inorganic nanofillers effectively delayed thermal decomposition by restricting polymer chain mobility and suppressing heat transfer through the matrix[22,31,32].

The second major degradation stage for PDA-PMF_{80} was observed around 428 °C, which can be attributed to the decomposition of ester linkages, ether moieties, and melamine-derived s-triazine

View Article Online
DOI: 10.1039/D6LF00075D

ring structures within the polymer backbone[22]. However, in the WO_3@PDA-PMF_{80} nanocomposite, this degradation region shifted further toward higher temperatures (~465 °C), demonstrating enhanced resistance against backbone decomposition. The delayed decomposition behavior suggests that WO_3 nanoparticles act as thermally stable inorganic barriers that retard the diffusion of volatile decomposition products and heat transfer during thermal degradation.

Further, PDA-PMF_{80} exhibited substantial mass loss (~85 wt.%) up to 600 °C due to extensive degradation of the polymer backbone, whereas the WO_3@PDA-PMF_{80} nanocomposite showed comparatively lower mass loss and improved thermal retention[7,12]. At 800 °C, PDA-PMF_{80} retained only ~5% residual char, while WO_3@PDA-PMF_{80} retained approximately ~12% residue, confirming the successful incorporation and homogeneous dispersion of thermally stable WO_3 nanofillers within the polymer matrix. The increased char residue indicates the formation of a more compact and thermally resistant structure in the nanocomposite system.

The enhanced thermal stability of WO_3@PDA-PMF_{80} may be attributed to the combined effects of: (i) strong interfacial interactions between WO_3 nanoparticles and the PDA-PMF_{80} polymer network, (ii) restriction of segmental mobility of polymer chains caused by uniformly dispersed nanofillers, and (iii) the barrier effect generated by WO_3 nanoparticles, which suppresses the transfer of heat and volatile degradation products during thermal decomposition. Similar thermal stabilization behavior has also been reported in Fe_3O_4 and RGO-reinforced alkyd nanocomposite coatings, where inorganic nanofillers filled interstitial voids within the cross-linked matrix and enhanced char-forming ability[22,31,32].

Moreover, the higher residual char formation and delayed decomposition temperatures of WO_3@PDA-PMF_{80} are beneficial for corrosion-protective applications, as the compact thermally

View Article Online
DOI: 10.1039/D6LF00075D

stable char layer can act as an effective barrier against the diffusion of corrosive ions and oxidative species at elevated temperatures.

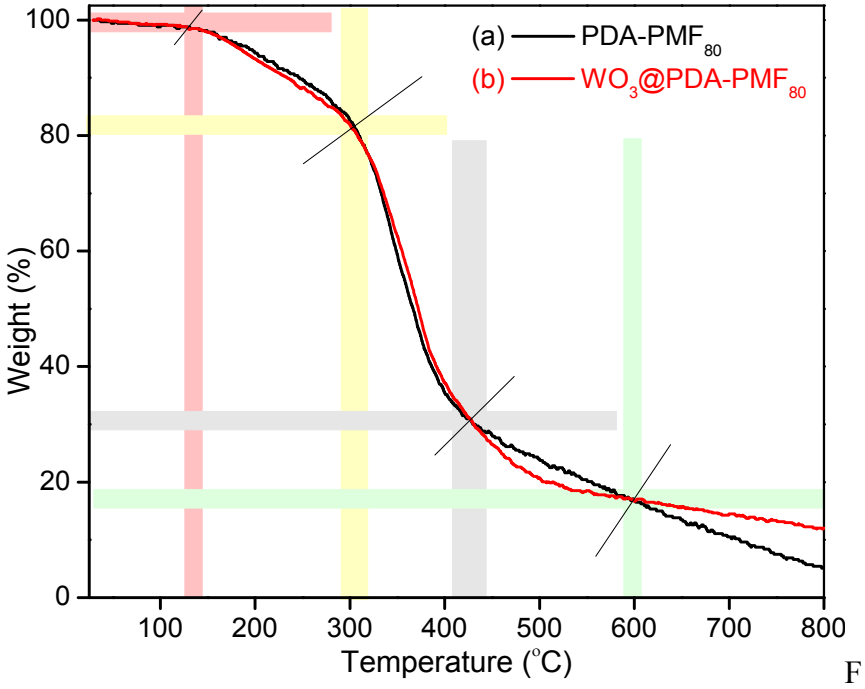

F

Figure-3 TGA thermograms of (a) PMF_{80}-cured alkyd (PDA-PMF_{80}) and (b) WO_3-dispersed PDA-PMF_{80} nanocomposite (WO_3@PDA-PMF_{80}).

3.4 TEM analysis

The morphological behavior of WO_3 nanoparticles and their dispersion within the PDA matrix were examined using the TEM microscopic technique, as illustrated in Figure-4. Figure-4a reveals that the synthesized WO_3 nanoparticles exhibit a dark-contrast, hemispherical morphology, confirming their well-defined shape and nanoscale structure[33]. In the WO_3@PDA-PMF_{80} nanocomposite (Figure-4b), the hemispherical WO_3 nanofillers are uniformly distributed throughout the PDA matrix without noticeable agglomeration. The dark circular regions of varying sizes correspond to WO_3 nanoparticles embedded within the polymer matrix, indicating their homogeneous dispersion and successful incorporation into the PDA-PMF_{80} network. The

View Article Online
DOI: 10.1039/D6LF00075D

uniform distribution of WO_3 nanofillers within the matrix is expected to promote strong interfacial interactions between the inorganic nanoparticles and the organic polymer network. Such homogeneous dispersion plays a crucial role in enhancing the overall performance of the WO_3@PDA-PMF_{80} nanocomposite, particularly by improving its Physicomechanical strength, thermal stability, and barrier properties [31].

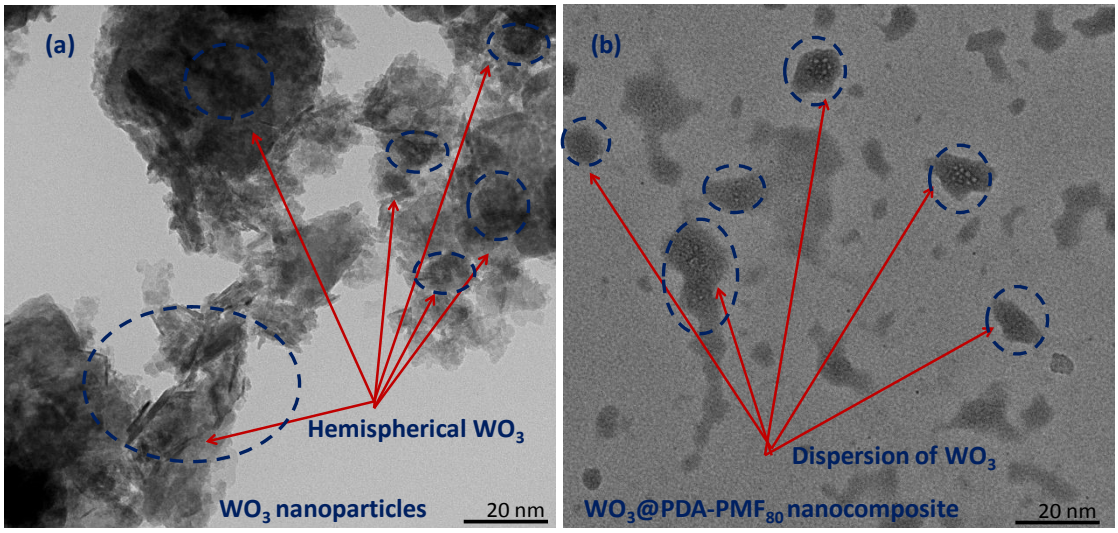

Figure-4 TEM micrographs of (a) WO_3 nanoparticles and (b) WO_3 nanofiller-dispersed PDA-PMF_{80} nanocomposites (WO_3@PDA-PMF_{80}).

3.5 Physicochemical and physico-mechanical characterization of PDA-nanocomposites

The physicochemical and Physico-mechanical properties of pristine PDA, PDA-PMF_{80}, and WO_3@PDA-PMF_{80} nanocomposite coatings were systematically evaluated using standard ASTM methods (Table S-1, Table S-2, and Figure-5). The specific gravity and refractive index showed a gradual increase in the order: PDA < PDA-PMF_{80} < WO_3@PDA-PMF_{80} (Table S-1). This progressive enhancement can be attributed to the incorporation of polar functionalities within the PDA matrix and the presence of WO_3 nanofillers, which promote increased crosslinking density and formation of compact, well-adhered coatings at the coating-CS

View Article Online
DOI: 10.1039/D6LF00075D

interface. The WO_3@PDA-PMF_{80} nanocomposite exhibited the highest values, indicating the formation of a homogeneous, dense, and highly cross-linked network structure with improved gloss characteristics. However, a continuous decrease in dry-to-touch (DTT) and dry-to-hard (DTH) times (Table S-2) was observed with nanofiller incorporation, which may be attributed to enhanced interfacial interactions between the WO_3 nanoparticles and the PDA matrix, accelerating curing and network formation. A slight increase in coating thickness was recorded in the order PDA (84.6 ± 0.55 μm) < PDA-PMF_{80} (89.2 ± 0.84 μm) < WO_3@PDA-PMF_{80} (91.0 ± 0.71 μm) (Table S-2), possibly due to the incorporation and dimensional contribution of WO_3 nanofillers within the polymer matrix. All coatings successfully passed impact resistance (250 $lb.inch^{-1}$) and bending (1/8″ mandrel) tests without rupture or cracking (Table S-2), confirming their excellent flexibility and mechanical integrity. A significant improvement in scratch hardness was observed, increasing from 5.5 kg (PDA) to 10.5 kg (PDA-PMF_{80}) and 12.0 kg (WO_3@PDA-PMF_{80}), respectively (Table S-2). This enhancement indicates improved load-bearing capacity and superior elastic-plastic deformation behavior at the coating-metal interface [26].

Although, overall enhancement in physicochemical and physico-mechanical properties of the WO_3@PDA-PMF_{80} nanocomposite coatings can be attributed to: (i) strong interfacial interactions between WO_3 nanofillers and the PDA matrix; (ii) the presence of pendant polar functional groups that improve adhesion at the coating/metal interface; (iii) effective occupation of interstitial sites by WO_3 nanoparticles within the polymer network; and (iv) improved elastic and plastic energy dissipation mechanisms [31]. The homogeneous dispersion of WO_3 nanofillers generates strong interlocking and cementing effects within the matrix, forming a compact barrier structure that promotes a tortuous (zigzag) diffusion pathway for corrosive ions at the coating-

View Article Online
DOI: 10.1039/D6LF00075D

metal interface [7,12,26]. In addition to that, the optical micrographs of PDA and its nanocomposite coatings reveal no peelings or cracks (Table S-2 and Figure-5). The crack-free cross-hatch square test of pristine PDA, PDA-PMF_{80}, and WO_3@PDA-PMF_{80} nanocomposite coatings suggests an excellent adhesion at the coatings-CS interface [14].

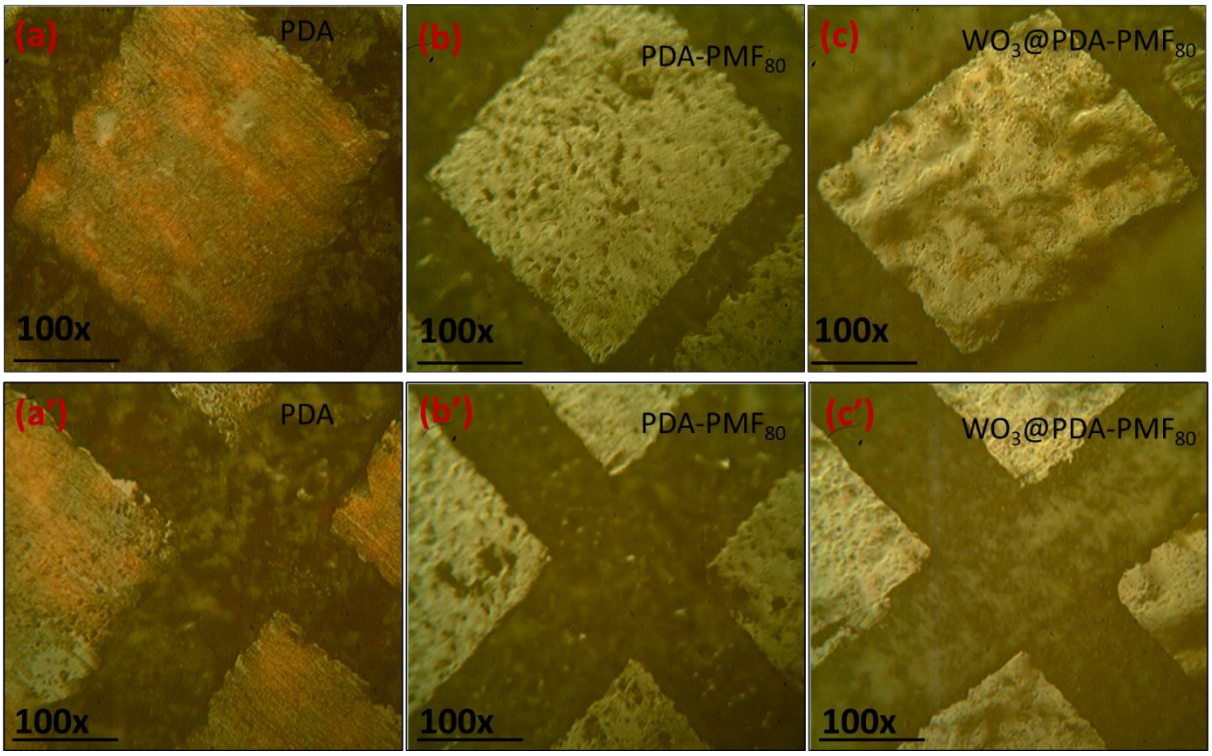

Figure-5 Optical micrographs of the cross-hatch square adhesion test for (a, a′) PDO-based alkyd (PDA), (b, b′) PMF_{80}-cured PDA (PDA-PMF_{80}), and (c, c′) WO_3-dispersed PDA-PMF_{80} nanocomposite (WO_3@PDA-PMF_{80}) coatings.

3.6 Contact angle study

The study on the contact angles (CAs) of PDA, PDA-PMF_{80}, and WO_3@PDA-PMF_{80} nanocomposite coatings demonstrates the materials' hydrophobic properties, which were measured using a CCD camera (PHOENIX 300 CA analyzer). Figure-6a demonstrates that the pristine PDA coating exhibited a contact angle of 89.70 ± 0.36°, indicating a relatively moderate

View Article Online
DOI: 10.1039/D6LF00075D

level of hydrophobicity. Upon curing with PMF, the PDA-PMF_{80} matrix showed a slightly increased contact angle of 92.31 ± 0.22°, suggesting an improvement in surface hydrophobicity due to enhanced crosslinking density and reduced surface polarity. Notably, the incorporation of WO_3 nanofillers into the PDA-PMF_{80} matrix significantly increased the contact angle to 108.74 ± 0.20°, indicating a marked enhancement in hydrophobicity. The progressive increase in contact angle follows the order: PDA (89.70 ± 0.36°) < PDA-PMF_{80} (92.31 ± 0.22°) < WO_3@PDA-PMF_{80} (108.74 ± 0.20°), confirming that the WO_3-reinforced nanocomposite possesses the most hydrophobic surface. The enhancement in hydrophobicity upon addition of WO_3 nanoparticles can be attributed to their effective integration and uniform dispersion within the polymer matrix, which increases surface roughness and generates nano-scale asperities on the coating surface. These hierarchical surface features facilitate air entrapment at the solid-liquid interface, thereby reducing the effective contact area between water droplets and the coating surface. This behavior is leading to an increased apparent contact angle and improved water-repellent performance of the WO_3@PDA-PMF_{80} nanocomposite coating [34,35].

View Article Online
DOI: 10.1039/D6LF00075D

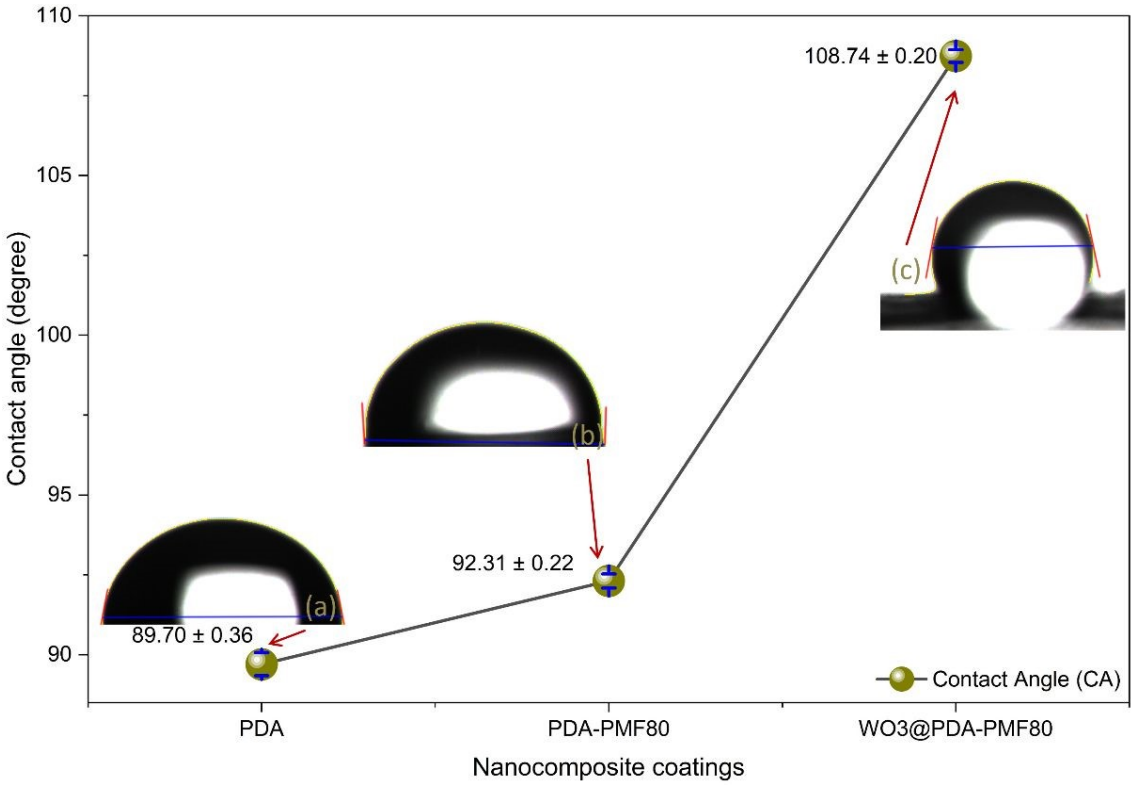

Figure-6 Water contact angle images of (a) PDA, (b) PDA-PMF_{80}, and (c) WO_3@PDA-PMF_{80} coatings demonstrating enhanced hydrophobicity.

3.7 EC resistance performances of the PDA, PDA-PMF_{80}, and WO_3@PDA-PMF_{80} coatings

The PDA, PDA-PMF_{80}, and WO_3@PDA-PMF_{80} nanocomposite coatings were tested for their EC protection capabilities on CS specimens under a highly aggressive saline environment (5 wt. % aqueous NaCl solution) over an immersion period of 10 days. The EC resistance characteristics were systematically investigated using PDP and EIS techniques. These electrochemical methods were employed to assess key corrosion parameters, including I_{corr}, E_{corr}, R_{ct}, and η_i of the coatings in the saline medium[13,26].

View Article Online
DOI: 10.1039/D6LF00075D

3.7.1 PDP analysis

PDP measurements were carried out to evaluate the EC protection performance of uncoated (CS) and coated (PDA, PDA-PMF_{80}, and WO_3@PDA-PMF_{80}) specimens, after immersion in a saline environment (5 wt.% NaCl solution) for 10 days (Table-1 and Figure-7) [13]. The polarization curves were analyzed to determine the key parameters, including corrosion rate, E_{corr}, I_{corr}, and η_i. The η_i of the coated systems was calculated using Equation (1) [7,14,26]

$$\eta i\ (\%)\ =\ (I'corr - Icorr)/I'corr \times 100 \qquad \textbf{(1)}$$

Where;

where I'_{corr} represents the corrosion current density of bare CS and I_{corr} corresponds to the corrosion current density of the coated specimens.

The obtained results reveal that corrosion resistance is predominantly governed by the barrier characteristics of the coating, interfacial adhesion strength, and suppression of electrochemical reactions at the coating-metal interface. Compared with bare CS, all coated samples exhibit significantly reduced I_{corr} values and lower corrosion rates, indicating effective mitigation of anodic metal dissolution and cathodic reduction reactions [29]. On the first day of immersion, the I_{corr} values followed the order: CS (4.42×10^{-4} A cm^{-2}) > PDA (1.73×10^{-7} A cm^{-2}) > PDA-PMF_{80} (1.56×10^{-7} A cm^{-2}) > WO_3@PDA-PMF_{80} (4.14×10^{-8} A cm^{-2}). After prolonged exposure, the I_{corr} values remained substantially lower for the composite coatings, particularly for WO_3@PDA-PMF_{80} (6.94×10^{-8} A cm^{-2}), confirming sustained electrochemical stability[26]. The E_{corr} values provide insight into the thermodynamic tendency of corrosion reactions. A shift toward more noble potential generally reflects improved corrosion resistance. After 10 days of immersion, the E_{corr} values were observed as follows: PDA (−0.4858 V), PDA-PMF_{80} (−0.5280 V), and WO_3@PDA-PMF_{80} (−0.5590 V). Although variations in E_{corr} were recorded, the

View Article Online
DOI: 10.1039/D6LF00075D

substantial decrease in I_{corr} remains the dominant indicator of enhanced corrosion protection. The polarization behavior demonstrates that incorporation of WO_3 nanofillers effectively suppresses charge transfer processes and improves barrier performance. The superior protection performance of WO_3@PDA-PMF_{80} nanocomposite coatings can be attributed to the homogeneous dispersion of WO_3 nanoparticles within the highly crosslinked PDA-PMF_{80} matrix. The dense polymeric network acts as a robust physical barrier, restricting the permeation of water molecules and aggressive chloride ions toward the metal surface. Additionally, ester and amide functionalities promote strong interfacial adhesion, while the presence of well-distributed nanofillers generates tortuous diffusion pathways that significantly delay electrolyte ingress. These combined effects minimize metal dissolution and enhance corrosion resistance, consistent with Faraday's law [36,37]. Based on PDP analysis, the corrosion rate values of the coated systems followed the trend: PDA (2.11×10^{-3} to 2.01×10^{-3}), PDA-PMF_{80} (2.29×10^{-3} to 1.80×10^{-3}), and WO_3@PDA-PMF_{80} (8.06×10^{-4} to 4.81×10^{-4}). The calculated corrosion protection efficiencies were 99.960% for PDA, 99.964% for PDA-PMF_{80}, and 99.990% for WO_3@PDA-PMF_{80}. These findings confirm that the WO_3-reinforced nanocomposite coating exhibits outstanding corrosion resistance and an excellent barrier characteristics in aggressive saline environments[12,26]

Table 1: PDP and EIS parameters of PDA and its nanocomposite coatings.

Sample	**I_{corr} (Acm^{-2})**	**E_{corr} (v)**	**Corrosion Rate (mpy)**	**η_i**
CS	4.42 x 10^{-4}	-0.38999	5.13	**…..**
1st day of immersion				
PDA	1.82 x 10^{-7}	-0.36252	2.11 x10^{-3}	**99.958**
PDA-PMF_{80}	1.97 x 10^{-7}	-0.53307	2.29 x 10^{-3}	**99.955**
WO_3@PDA-	6.94 x 10^{-8}	-0.65795	8.06 x 10^{-4}	**99.984**

View Article Online
DOI: 10.1039/D6LF00075D

PMF_{80}				
10^{th} day of immersion				
PDA	1.73 x 10^{-7}	-0.48589	2.01 x10^{-3}	**99.960**
PDA-PMF_{80}	1.56 x 10^{-7}	-0.52804	1.80 x 10^{-3}	**99.964**
WO_3@PDA-PMF_{80}	4.14 x 10^{-8}	-0.55904	4.81 x10^{-4}	**99.990**

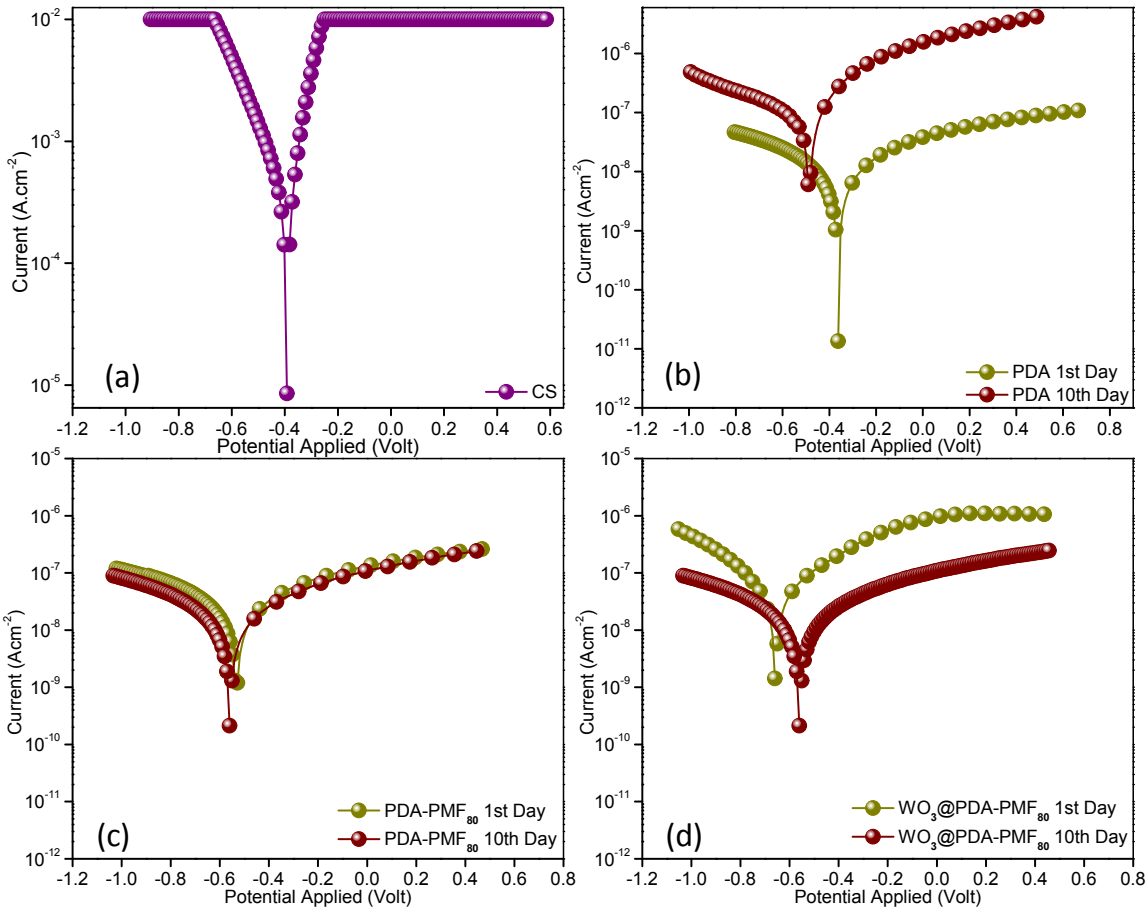

Figure-7 PDP curves illustrating the EC behavior of coated specimens: (a) PDA, (b) PDA-PMF_{80}, and (c) WO_3@PDA-PMF_{80} nanocomposite coatings under 5 wt.% NaCl solution for 10 days of immersion.

View Article Online
DOI: 10.1039/D6LF00075D

3.7.2 EIS analysis

EIS was employed to further examine the corrosion protection performance of uncoated (CS) and coated (PDA, PDA-PMF_{80}, and WO_3@PDA-PMF_{80}) specimens, after immersion in 5 wt.% NaCl solution for 10 days (Figure S-2 and Figure-8). The impedance response was analyzed through Nyquist plots (Z′ vs. Z″), Bode modulus plots (log |Z| vs. log f), and phase angle plots (phase angle vs. log f). The corresponding electrochemical equivalent circuit (EEC) models used to fit the experimental data are presented in Figure-8f [7]. The proposed circuits consist of solution resistance (R_s) at the high-frequency intercept, along with coating pore resistance (R_{pore}), charge transfer resistance (R_{ct}), coating capacitance (C_c), and double-layer capacitance (C_{dl}) at lower frequency regions.

The Nyquist spectra (Figure 8a–c) provide insight into the time-dependent evolution of coating performance. On the first day of immersion (Figure-8a), PDA and its nanocomposite coatings exhibited capacitive semicircles characteristic of barrier-type coatings. The presence of two distinguishable time constants, particularly evident in Figure-8b, suggests two electrochemical processes: one associated with the coating layer at high frequencies and another corresponding to interfacial charge transfer reactions at lower frequencies. This behavior is well represented by the equivalent circuit $R_s(C_c(R_{pore}(C_{dl}R_{ct})))$ shown in Figure-8f. With increasing immersion time (1st to 5th day), PDA and PDA-PMF_{80} coatings showed a gradual reduction in R_{pore} and R_{ct}, accompanied by an increase in C_{dl}. This trend indicates progressive electrolyte penetration through micro-defects and subsequent initiation of interfacial corrosion processes. In contrast, incorporation of WO_3 nanofillers into the PDA-PMF_{80} matrix significantly enhanced coating integrity. The WO_3@PDA-PMF_{80} system displayed higher R_{pore} values and relatively stable capacitance behavior, reflecting improved resistance against electrolyte ingress. Even after 10

View Article Online
DOI: 10.1039/D6LF00075D

days of exposure (Figure-8c), WO_3@PDA-PMF_{80} exhibited a dominant single capacitive loop with a comparatively larger semicircle diameter, indicating strong barrier performance and minimal interfacial degradation. An increase in semicircle diameter is directly associated with higher polarization resistance, confirming improved corrosion resistance of the nanocomposite coatings. The enhanced performance of WO_3@PDA-PMF_{80} can be attributed to uniform nanofiller dispersion, which increases tortuosity and restricts ionic transport. In comparison, PDA and PDA-PMF_{80} coatings exhibited partial deterioration beyond the 5th day of immersion, suggesting the onset of localized corrosion processes. The overall corrosion resistance followed the order: PDA < PDA-PMF_{80} < WO_3@PDA-PMF_{80}. Comparative evaluation with recently reported systems further highlights the excellent barrier efficiency of the WO_3@PDA-PMF_{80} nanocomposite coatings (Table S-4).

Moreover, the Bode plots (Figure S-2 and Figure 8d-e) further corroborate these findings. In the high-frequency region, all coatings displayed capacitive behavior corresponding to intact film properties, whereas the mid-frequency to low-frequency regions reflected charge transfer processes at the coating-metal interface[22]. The low-frequency impedance modulus (|Z|0.01 Hz) of WO_3@PDA-PMF_{80} was significantly higher than that of pristine PDA, indicating enhanced resistance to ionic conduction. Although a general decrease in |Z|0.01 Hz was observed with prolonged immersion for all systems, the magnitude of reduction was smallest for WO_3@PDA-PMF_{80}, confirming its superior enduring stability in saline medium. The impedance performance trend was consistent with: PDA < PDA-PMF_{80} < WO_3@PDA-PMF_{80}.

Phase angle diagrams provide additional insight into coating degradation and delamination behavior. The WO_3@PDA-PMF_{80} coating maintained higher phase angle values (approaching capacitive behavior) in the middle- and high-frequency regions throughout immersion, indicating

View Article Online
DOI: 10.1039/D6LF00075D

minimal structural deformation and sustained barrier properties. In contrast, lower phase angle values for PDA coatings suggest increased heterogeneity and electrolyte penetration. The overall phase angle response followed the sequence: CS < PDA < PDA-PMF_{80} < WO_3@PDA-PMF_{80}, confirming the superior electrochemical stability of the WO_3-reinforced nanocomposite coating in 5 wt.% NaCl solution.

However, the breakpoint frequency (f_b), defined as the frequency corresponding to a phase angle of 45°, was also evaluated to assess coating defect developmen[7,29,38]. Since f_b is directly related to the effective defect area of a coating, an increase in f_b indicates progressive coating degradation. For PDA and PDA-PMF_{80} coatings, f_b shifted toward higher frequencies with increasing immersion time, suggesting growing defect density and interfacial delamination. In contrast, WO_3@PDA-PMF_{80} exhibited only a marginal shift in f_b, reflecting minimal defect propagation. The presence of WO_3 nanofillers effectively reduces ion diffusion pathways and delays coating failure, thereby maintaining high protection efficiency over prolonged immersion [12,26].

View Article Online
DOI: 10.1039/D6LF00075D

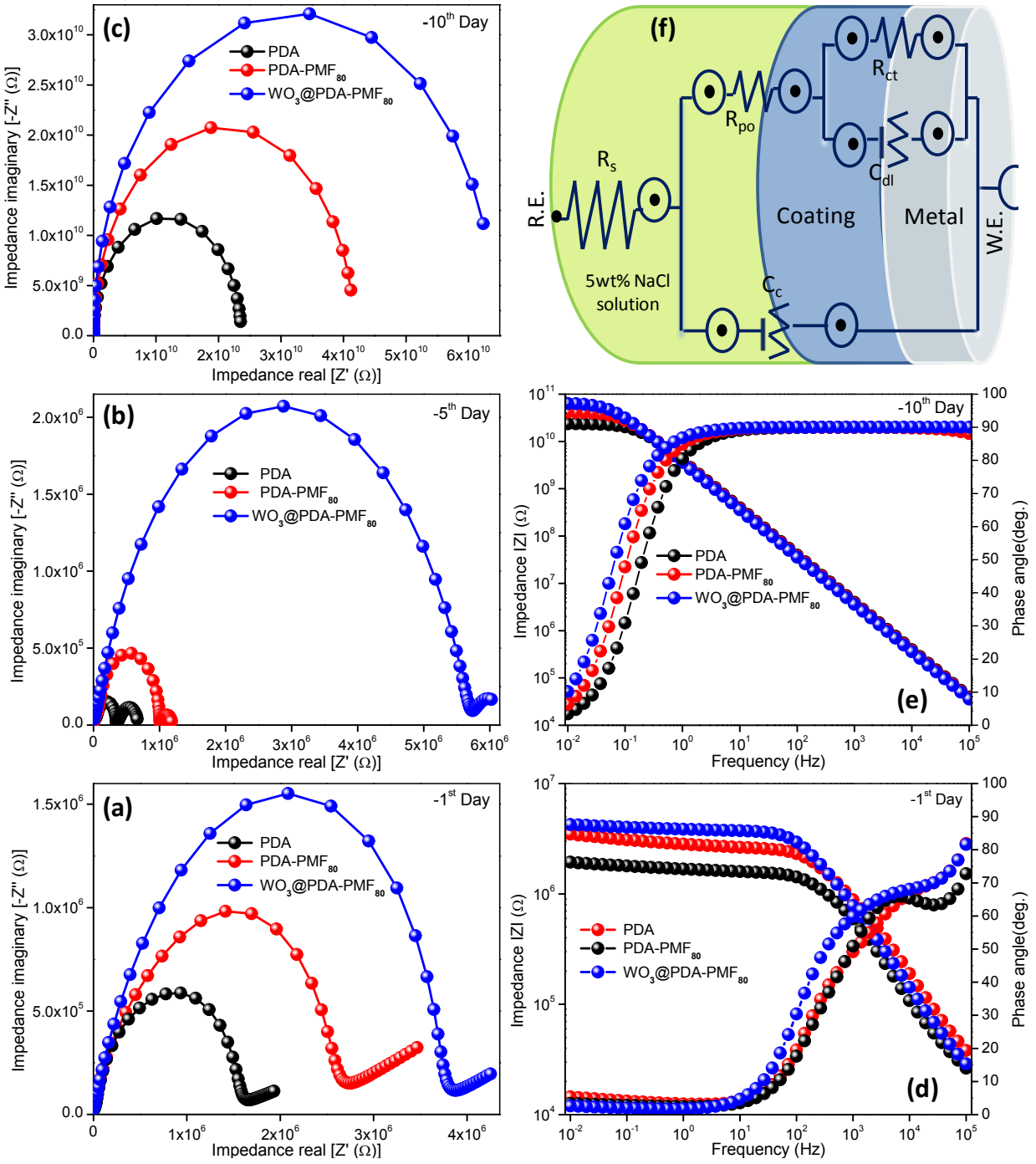

Figure-8 Nyquist plots (a–c), Bode impedance modulus and phase angle plots (d, e), and the equivalent circuit model (f) illustrating the EC protection performance of PDA, PDA-PMF_{80}, and WO_3@PDA-PMF_{80} nanocomposite coatings under 5 wt.% NaCl solution for 10 days of immersion.

View Article Online
DOI: 10.1039/D6LF00075D

3.7.3 AFM Surface Morphology and Roughness Analysis

To further investigate the surface characteristics and morphological stability of the developed coatings, Atomic Force Microscopy (AFM) analysis was carried out before and after corrosion exposure[39]. The AFM studies were performed to evaluate the surface topography and roughness behavior of PDA, PDA-PMF_{80}, and WO_3@PDA-PMF_{80} coatings (Figure 9 and Table 2).

The AFM results revealed distinct differences in the surface morphology of the investigated coatings. Prior to corrosion exposure, the pristine PDA coating exhibited comparatively higher surface roughness, indicating a relatively heterogeneous and uneven surface. In contrast, the PDA-PMF_{80} and WO_3@PDA-PMF_{80} coatings displayed smoother, denser, and more uniform surface morphology due to enhanced crosslinking and improved dispersion of WO_3 nanofillers within the polymer matrix. Among all investigated samples, the WO_3@PDA-PMF_{80} nanocomposite coating exhibited the lowest mean roughness (R_a) and Route mean square roughness (R_s) values, confirming the formation of a compact and homogeneous protective coating layer.

After immersion in the corrosive in 5 wt. % aqueous NaCl solution environment, all coatings exhibited an increase in surface roughness due to electrolyte penetration and corrosion-induced surface degradation. However, the WO_3@PDA-PMF_{80} nanocomposite coating showed the smallest increase in roughness values compared to its PDA and PDA-PMF_{80} coatings, indicating superior surface stability and improved resistance against corrosive attack. The comparatively lower roughness variation suggests that the uniformly dispersed WO_3 nanofillers enhanced the compactness and barrier characteristics of the coating matrix, thereby minimizing the formation of micro-defects and surface deterioration during corrosion exposure.

View Article Online
DOI: 10.1039/D6LF00075D

Table 2. Average surface roughness parameters obtained from AFM analysis of PDA, PDA-PMF_{80}, and WO_3@PDA-PMF_{80} coatings before and after corrosion exposure.

Coating Samples	Mean Roughness R(a) ± S.D.	RMS Roughness R(s) ± S.D.
Before Corrosion		
PDA	21.1 ± 1.12	26.7 ± 1.5
PDA-PMF_{80}	5.7 ± 0.4	14.2 ± 0.9
WO_3@PDA-PMF_{80}	3.2 ± 0.2	5.1 ± 0.3
After Corrosion		
PDA	26.6 ± 1.8	48.9 ± 2.7
PDA-PMF_{80}	12.1 ± 0.7	20.0 ± 1.2
WO_3@PDA-PMF_{80}	4.6 ± 0.3	6.3 ± 0.4

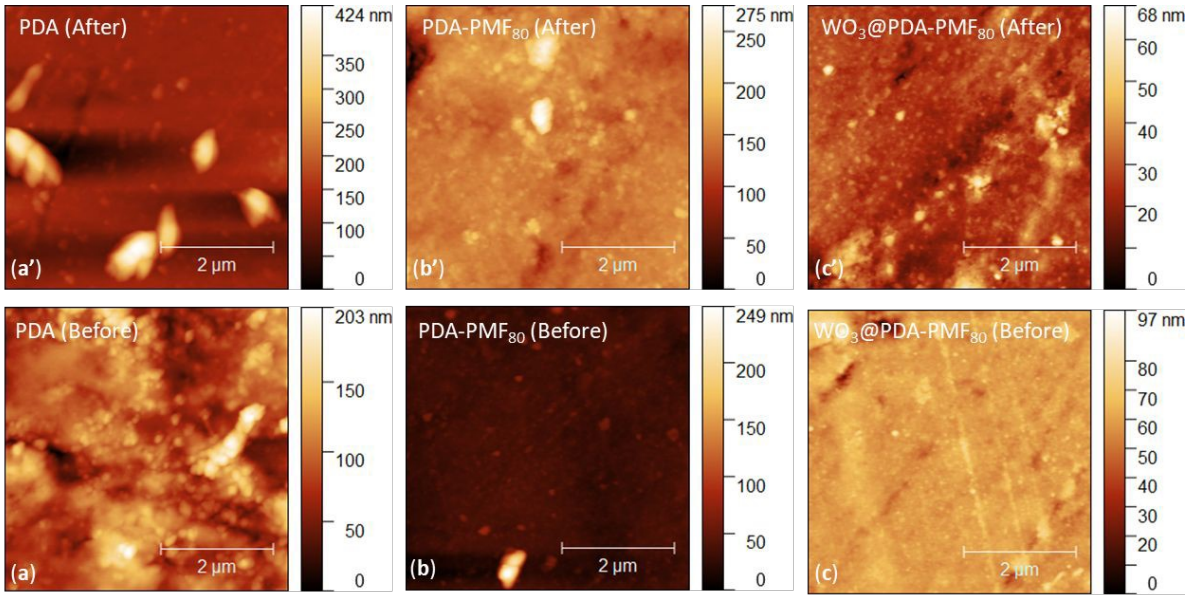

Figure 9. Atomic Force Microscopy (AFM) surface topography images of PDA, PDA-PMF80, and WO3@PDA-PMF80 coatings recorded (a–c) before and (a′–c′) after corrosion exposure, illustrating the changes in surface morphology and roughness characteristics after immersion in a harsh saline corrosive environment.

3.7.4 EC protection mechanism

View Article Online
DOI: 10.1039/D6LF00075D

The EC protection mechanism of PDA, PDA-PMF_{80}, and WO_3@PDA-PMF_{80} coatings in 5 wt.% NaCl medium is predominantly governed by synergistic barrier effects and interfacial electrochemical processes, as illustrated in Figure 10. The pristine PDA coating exhibits comparatively lower protective efficiency than its nanocomposite counterpart, primarily due to limited crosslink density and weaker interfacial adhesion, which facilitate electrolyte permeation and subsequent initiation of corrosion reactions at the coating-metal interface [15,40]. The presence of microvoids and structural heterogeneity in PDA coatings promotes rapid ingress of chloride ions, thereby accelerating degradation.

In contrast, the WO_3@PDA-PMF_{80} nanocomposite coating demonstrates markedly enhanced corrosion resistance. This improvement arises from multiple cooperative mechanisms: (i) suppression of anodic and cathodic reactions through interfacial redox stabilization, (ii) formation of an effective physical barrier layer that restricts ionic transport, (iii) strong electrostatic interactions between pendant polar functional groups in the polymer matrix and the positively charged metal surface, and (iv) development of a passivating layer at the interface via auto-oxidative processes [14,41,42]. Functional moieties such as carboxyl, hydroxyl, ester, and unsaturated linkages enhance interfacial bonding and reduce permeability, thereby limiting diffusion of aggressive chloride ions and increasing ionic resistance within the coating matrix [14,43].

The superior protection performance of WO_3@PDA-PMF_{80} can further be attributed to its highly crosslinked and compact polymeric network, which generates a dense microstructure with improved mechanical integrity. The well-dispersed WO_3 nanofillers introduce interlocking and reinforcing effects within the matrix, while simultaneously creating tortuous (zigzag) diffusion pathways that significantly delay electrolyte penetration [12]. Additionally, the establishment of a

View Article Online
DOI: 10.1039/D6LF00075D

synergistic dual barrier layer comprising the organic coating matrix and a stabilized interfacial region enhances electrochemical stability. Such adaptive interfacial behavior supports classification of the WO_3-reinforced system as a multifunctional or smart protective coating [42,44]. The corrosion resistance performance of the investigated systems follows the order: PDA < PDA-PMF_{80} < WO_3@PDA-PMF_{80}, confirming that incorporation of WO_3 nanofillers significantly improves barrier efficiency, interfacial stability, and enduring protection in saline environments.

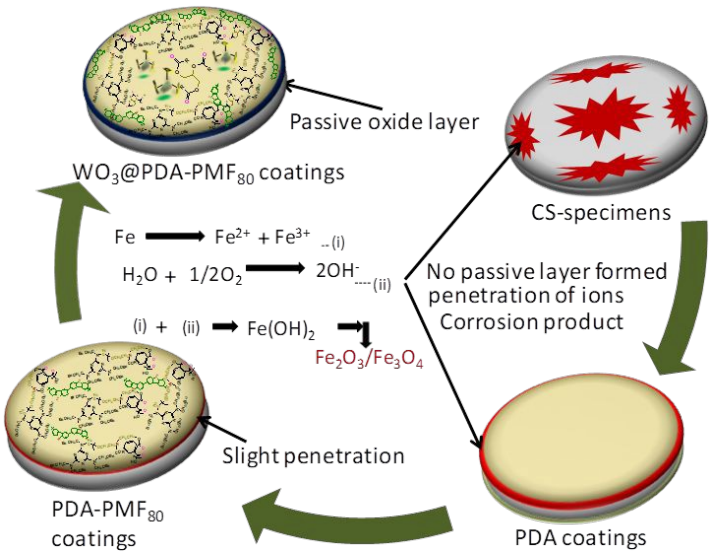

Figure-10 Graphical representation of the EC resistance mechanism of PDA, PDA-PMF_{80}, and WO_3@PDA-PMF_{80} nanocomposite coatings.

Conclusions

Bio-based PDA alkyd and its WO_3-reinforced nanocomposite coatings were successfully synthesized through an environmentally friendly *in-situ* polymerization approach and applied onto carbon steel (CS) substrates using brush coating technique. The developed coatings were systematically characterized using FTIR, NMR, TGA, TEM, AFM, contact angle analysis, PDP, and EIS techniques to investigate their structural, thermal, surface, and anticorrosive properties.

View Article Online
DOI: 10.1039/D6LF00075D

The incorporation of PMF_{80} and uniformly dispersed WO_3 nanofillers significantly improved the compactness, crosslink density, barrier characteristics, and hydrophobic behavior of the PDA matrix. AFM analysis further revealed relatively homogeneous surface morphology and lower roughness variation after corrosion exposure for the WO_3@PDA-PMF_{80} nanocomposite coating, indicating improved surface stability and resistance toward electrolyte penetration. Thermal studies demonstrated enhanced thermal stability of the nanocomposite coatings up to approximately 150 °C.

Electrochemical investigations in 5 wt.% NaCl solution confirmed that the WO_3@PDA-PMF_{80} coating exhibited superior corrosion protection performance compared with PDA and PDA-PMF_{80} coatings, showing an E_{corr} of −0.52804 V, an I_{corr} of 1.56×10^{-7} A cm^{-2}, a corrosion rate of 4.81×10^{-4} mpy, and corrosion protection efficiency of 99.99% under the investigated exposure conditions. The enhanced performance is mainly attributed to the improved crosslinked polymer network, homogeneous WO_3 dispersion, and the formation of tortuous diffusion pathways that effectively restricted the ingress of corrosive species toward the coating/substrate interface. Although, the developed WO_3@PDA-PMF_{80} nanocomposite coating demonstrates promising potential as a sustainable high-performance anticorrosive coating material for advanced protective coating applications.

Author's Information

[1]Abu Darda*

Department of Materials Science and Engineering, Indian Institute of Technology Delhi

E-mail address: *abudardazilli@gmail.com*

*Corresponding Author

[2]Nitya Nand Gosvami

View Article Online
DOI: 10.1039/D6LF00075D

Department of Materials Science and Engineering, Indian Institute of Technology Delhi
E-mail address: ngosvami@mse.iitd.ac.in

[3]Weqar Ahmad Siddiqi
Department of Applied Sciences and Humanities, Jamia Millia Islamia, New Delhi, India
E-mail address: wsiddiqui@jmi.ac.in

Conflict of Interest

The author(s) have declared no competing financial interests.

Acknowledgments

One of the authors, Dr. Abu Darda, gratefully acknowledges the Department of Chemistry, Jamia Millia Islamia, for access to the electrochemical facilities used for corrosion evaluation.

Supporting Information

The Supporting Information contains: Figure S-1. FTIR spectra confirming the functional characteristics of WO_3 nanoparticles, Figure S-2. (a) Nyquist and (b) Bode and phase angle plots of uncoated carbon steel (CS) in 5 wt.% NaCl solution, Table S-1. Physicochemical parameters of PDA, PDA-PMF_{80}, and WO_3@PDA-PMF_{80} nanocomposite coatings, Table S-2. Physicomechanical parameters of PDA, PDA-PMF_{80}, WO_3@PDA-PMF_{80} nanocomposite coatings, Table S-3. Thermogravimetric parameters of these coatings, and Table-4. Comparison of anticorrosive performance of WO_3@PDA-PMF_{80} nanocomposite coatings with reported systems in the literature, and Section S-1. FTIR spectroscopic analysis of WO_3 nanoparticles.

View Article Online
DOI: 10.1039/D6LF00075D

References:

1. Verma, C. *et al.* Principles and theories of green chemistry for corrosion science and engineering: design and application. *Green Chemistry* **26**, 4270–4357 (2024).

2. Zagalskaya, A., Chaudhary, P. & Alexandrov, V. Corrosion of Electrochemical Energy Materials: Stability Analyses Beyond Pourbaix Diagrams. *Journal of Physical Chemistry C* **127**, 14587–14598 (2023).

3. Li, X. *et al.* Nanomaterials Reinforced Antifouling Coatings: From Strategic Design to Potential Applications. *Advanced Materials* **14795**, 1–46 (2025).

4. Aljibori, H., Al-Amiery, A. & Isahak, W. N. R. *Advancements in Corrosion Prevention Techniques*. *Journal of Bio- and Tribo-Corrosion* vol. 10 (Springer International Publishing, 2024).

5. Douglas, L. D. *et al.* A Materials Science Perspective of Midstream Challenges in the Utilization of Heavy Crude Oil. *ACS Omega* **7**, 1547–1574 (2022).

6. Chen, F. *et al.* Robust and durable liquid-repellent surfaces. *Chemical Society Reviews* **51**, 8476–8583 (2022).

7. Pathan, S. & Ahmad, S. Synergistic Effects of Linseed Oil Based Waterborne Alkyd and 3-Isocynatopropyl Triethoxysilane: Highly Transparent, Mechanically Robust, Thermally Stable, Hydrophobic, Anticorrosive Coatings. *ACS Sustainable Chemistry and Engineering* **4**, 3062–3075 (2016).

8. Pathan, S. & Ahmad, S. Green and sustainable anticorrosive coating derived from waterborne linseed alkyd using organic-inorganic hybrid cross linker. *Progress in Organic Coatings* **122**, 189–198 (2018).

9. Rajput, C. V., Sastry, N. V. & Chikhaliya, N. P. *Vegetable Oils Based Precursors:*

View Article Online
DOI: 10.1039/D6LF00075D

Modifications and Scope for Futuristic Bio-Based Polymeric Materials. *Journal of Polymer Research* vol. 30 (Springer Netherlands, 2023).

10. Gogoi, P., Boruah, M., Sharma, S. & Dolui, S. K. Blends of Epoxidized Alkyd Resins Based on Jatropha Oil and the Epoxidized Oil Cured with Aqueous Citric Acid Solution: A Green Technology Approach. (2015) doi:10.1021/sc500627u.
11. Sharmin, E., Zafar, F., Akram, D., Alam, M. & Ahmad, S. Recent advances in vegetable oils based environment friendly coatings: A review. *Industrial Crops and Products* **76**, 215–229 (2015).
12. Darda, A., Khatoon, H., Siddiqi, W. A. & Ahmad, S. Polythiophene enveloped tungsten-oxide hybrid nanofillers dispersed oleo (Pithecellobium Dulce seed oil) polyurethane bi-functional nanocomposite coatings. *Progress in Organic Coatings* **172**, 107038 (2022).
13. Alkyd, W. s - Triazine Ring-Modi fi ed Waterborne Alkyd: Synthesis, Characterization, Antibacterial, and Electrochemical Corrosion Studies. (2013).
14. Khatoon, H. & Ahmad, S. Vanadium Pentoxide-Enwrapped Polydiphenylamine/Polyurethane Nanocomposite: High-Performance Anticorrosive Coating. *ACS Applied Materials and Interfaces* **11**, 2374–2385 (2019).
15. Irfan, M. *et al.* Renewable Resource-Based Environmental Friendly Waterborne Polymeric Anticorrosive Nanocomposite Coatings. *Green Polymer Chemistry and Composites* 95–111 (2021) doi:10.1201/9781003083917-7.
16. Darda, A. & Siddiqi, W. A. Mechanically robust bifunctional hydrophobic polycarbazole-decorated multiwall carbon nanotube-Pithecellobium dulce oil polyester amide nanocomposite coatings: fabrication, characterization, anticorrosive and antimicrobial studies. *Journal of Materials Chemistry A* (2024) doi:10.1039/d4ta06332e.

View Article Online
DOI: 10.1039/D6LF00075D

17. Xavier, J. R. Effect of surface modified WO3 nanoparticle on the epoxy coatings for the adhesive and anticorrosion properties of mild steel. *Journal of Applied Polymer Science* **137**, 1–10 (2020).

18. Selim, M. S., Shenashen, M. A., Hashem, A. I. & El-Safty, S. A. Linseed oil-based alkyd/Cu 2 O nanocomposite coatings for surface applications. *New Journal of Chemistry* **42**, 10048–10058 (2018).

19. Darda, A. *et al.* The Next Generation Sustainable Polymers. *Green Polymer Chemistry and Composites* 19–31 (2021) doi:10.1201/9781003083917-2.

20. Bakshi, M. I., Khatoon, H. & Ahmad, S. Hydrophobic, Mechanically Robust Polysorbate-Enveloped Cerium Oxide-Dispersed Oleo-Polyetheramide Nanocomposite Coatings for Anticorrosive and Anti-Icing Applications. *Industrial and Engineering Chemistry Research* **59**, 6617–6628 (2020).

21. Khatoon, H., Iqbal, S., Irfan, M., Darda, A. & Rawat, N. K. A review on the production, properties and applications of non-isocyanate polyurethane: A greener perspective. *Progress in Organic Coatings* **154**, 106124 (2021).

22. Rahman, O. U., Bhat, S. I., Yu, H. & Ahmad, S. Hyperbranched Soya Alkyd Nanocomposite: A Sustainable Feedstock-Based Anticorrosive Nanocomposite Coatings. *ACS Sustainable Chemistry and Engineering* **5**, 9725–9734 (2017).

23. Sharmin, E. *et al.* Linseed oil polyol/ZnO bionanocomposite towards mechanically robust, thermally stable, hydrophobic coatings: A novel synergistic approach utilising a sustainable resource. *RSC Advances* **5**, 47928–47944 (2015).

24. Zeng, Y. *et al.* Sensors and Actuators B : Chemical Rapid and selective H 2 S detection of hierarchical ZnSnO 3 nanocages. *Sensors & Actuators: B. Chemical* **159**, 245–250 (2011).

View Article Online
DOI: 10.1039/D6LF00075D

25. Alam, S. *et al.* Ultrasensitive NOX Detection in Simulated Exhaled Air: Enhanced Sensing via Alumina Modification of In-Situ Grown WO3 Nanoblocks. *Chemistry - An Asian Journal* 4673–4680 (2019) doi:10.1002/asia.201900699.

26. Irfan, M., Bhat, S. I. & Ahmad, S. Reduced Graphene Oxide Reinforced Waterborne Soy Alkyd Nanocomposites: Formulation, Characterization, and Corrosion Inhibition Analysis. *ACS Sustainable Chemistry and Engineering* **6**, 14820–14830 (2018).

27. Acikbas, G., Calis Acikbas, N., Dizge, N. & Belibagli, P. Multi-functional ceramic glazes with nano ZnO/Cu–ZnO incorporation. *Ceramics International* **50**, 43800–43810 (2024).

28. Irfan, M., Bhat, S. I. & Ahmad, S. *Waterborne Reduced Graphene Oxide Dispersed Bio-Polyesteramide Nanocomposites: An Approach towards Eco-Friendly Anticorrosive Coatings*. *New Journal of Chemistry* vol. 43 (Royal Society of Chemistry, 2019).

29. Bakshi, M. I. & Ahmad, S. In situ synthesis of high-performance 4,4′-diaminodiphenylsulfone modified oleo-alkyd nanocomposite coatings: Role of hybrid nanofillers on physico-mechanical, hydrophobic and corrosion protective performance. *New Journal of Chemistry* **44**, 17924–17937 (2020).

30. Pathan, S. & Ahmad, S. Synthesis, characterization and the effect of the s-triazine ring on physico-mechanical and electrochemical corrosion resistance performance of waterborne castor oil alkyd. *Journal of Materials Chemistry A* **1**, 14227–14238 (2013).

31. Rahman, O. U. & Ahmad, S. Physico-mechanical and electrochemical corrosion behavior of soy alkyd/Fe3O4 nanocomposite coatings. *RSC Advances* **4**, 14936–14947 (2014).

32. Irfan, M., Bhat, S. I. & Ahmad, S. Reduced Graphene Oxide Reinforced Waterborne Soy Alkyd Nanocomposites: Formulation, Characterization, and Corrosion Inhibition Analysis. (2018) doi:10.1021/acssuschemeng.8b03349.

View Article Online
DOI: 10.1039/D6LF00075D

33. Huang, J., Kang, Y., Yang, T., Wang, Y. & Wang, S. Preparation of polythiophene/WO3 organic-inorganic hybrids and their gas sensing properties for NO2 detection at low temperature. *Journal of Natural Gas Chemistry* **20**, 403–407 (2011).

34. Ghosal, A. & Ahmad, S. High performance anti-corrosive epoxy-titania hybrid nanocomposite coatings. *New Journal of Chemistry* **41**, 4599–4610 (2017).

35. Salata, R., Pellegrene, B. & Soucek, M. Migration of fluorinated alkyd and fluorinated tung oil additives for partially self-stratifying coatings. *Progress in Organic Coatings* **133**, 406–417 (2019).

36. Kumar, D. *et al.* Diamond & Related Materials Effect of nanodiamond concentration on the electrochemical behavior of plasma sprayed titanium-nanodiamond nanocomposite coatings. *Diamond & Related Materials* **130**, 109419 (2022).

37. Talha, M., Wang, Q., Ma, Y. & Lin, Y. International Journal of Adhesion and Adhesives Self-assembled hybrid silane / ZnO coatings for corrosion protection of resorbable magnesium alloy. *International Journal of Adhesion and Adhesives* **120**, 103281 (2023).

38. Feng, P. X. *et al.* Constructing lignin functional coatings for intelligent protection through interface engineering technology: exhibiting excellent anti-corrosion and weather resistance. *Rare Metals* **44**, 6614–6625 (2025).

39. Madayag, J. V. M. *et al.* Fluoropolymer Coatings with Inhibitor-Laden Zinc Oxide Nanoparticles: Electrochemical Characterization and Monte Carlo Simulation. *ACS Applied Engineering Materials* (2025) doi:10.1021/acsaenm.5c00871.

40. Prasetya, N. B. A., Ajizan, A. I., Widodo, D. S., Ngadiwiyana, N. & Gunawan, G. Polyeugenol/graphene composite with excellent anti-corrosion coating properties. *Materials Advances* (2022) doi:10.1039/d2ma00875k.

View Article Online
DOI: 10.1039/D6LF00075D

41. Wang, H. *et al.* Stretchable and self-healing polyurethane coating with synergistic anticorrosion effect for the corrosion protection of stainless steels. *Progress in Organic Coatings* **164**, 106672 (2022).

42. Ahmad, S., Riaz, U. & Ashraf, S. M. Comparative study of polyaniline and poly(1-naphthylamine) dispersed oil polyurethane coatings. *Anti-Corrosion Methods and Materials* **55**, 308–316 (2008).

43. Aung, M. M., Li, W. J. & Lim, H. N. Improvement of Anticorrosion Coating Properties in Bio-Based Polymer Epoxy Acrylate Incorporated with Nano Zinc Oxide Particles. *Industrial and Engineering Chemistry Research* **59**, 1753–1763 (2020).

44. Riaz, U., Ashraf, S. M. & Ahmad, S. Comparative study of polyaniline and poly (1-naphthylamine) dispersed oil polyurethane coatings. (2010) doi:10.1108/00035590810913097.

View Article Online
DOI: 10.1039/D6LF00075D

Data Availability Statement:

The data supporting this study are available from the corresponding author upon reasonable request.